

## Research Article

# Analysis of Magnetohydrodynamic Micropolar Nanofluid Flow due to Radially Stretchable Rotating Disk Employing Spectral Method

Ayele Tulu 

Department of Mathematics, Ambo University, Ambo, Ethiopia

Correspondence should be addressed to Ayele Tulu; ayeletulu@gmail.com

Received 15 December 2022; Revised 24 January 2023; Accepted 2 February 2023; Published 24 February 2023

Academic Editor: Ghulam Rasool

Copyright © 2023 Ayele Tulu. This is an open access article distributed under the Creative Commons Attribution License, which permits unrestricted use, distribution, and reproduction in any medium, provided the original work is properly cited.

The present analysis is aimed at examining MHD micropolar nanofluid flow past a radially stretchable rotating disk with the Cattaneo-Christov non-Fourier heat and non-Fick mass flux model. To begin with, the model is developed in the form of nonlinear partial differential equations (PDEs) for momentum, microrotation, thermal, and concentration with their boundary conditions. Employing suitable similarity transformation, the boundary layer micropolar nanofluid flows governing these PDEs are transformed into large systems of dimensionless coupled nonlinear ordinary differential equations (ODEs). These dimensionless ODEs are solved numerically by means of the spectral local linearization method (SLLM). The consequences of more noticeable involved parameters on different flow fields and engineering quantities of interest are thoroughly inspected, and the results are presented via graph plots and tables. The obtained results confirm that SLLM is a stable, accurate, convergent, and computationally very efficient method to solve a large coupled system of equations. The radial velocity grows while the tangential velocity, temperature, and concentration distributions turn down as the value of the radial stretching parameter improves, and hence, in practical applications, radial stretching of the disk is helpful to advance the cooling process of the rotating disk. The occurrence of microrotation viscosity in microrotation parameters ( $A_1 - A_6$ ) declines the radial velocity profile, and the kinetic energy of the fluid is reduced to some extent far away from the surface of the disk. The novelty of the study is the consideration of microscopic effects occurring from the micropolar fluid elements such as micromotion and couple stress, the effects of non-Fourier's heat and non-Fick's mass flux, and the effect of radial stretching disk on micropolar nanofluid flow, heat, and mass transfer.

## 1. Introduction

The study of fluid flow with heat conveyed over the rotating disk surface has been receiving astonishing attention from researchers as a result of its various applications in the area of manufacturing industry and engineering such as in the rotating machinery field, thermal power generating systems, computer storage devices, geothermal industry, heat and mass exchanger, gas turbine rotators, medical machinery, chemical processes, air cleaning apparatus, and electronic device. The flow of fluid due to a rotating disk was initially studied by [1], and following him, different valuable studies on the theme of fluid flow induced by the rotating disk have been conducted and published by different researchers up to

these days. The flow of nanofluid via a revolving porous disk was investigated by [2], while entropy investigation in magnetohydrodynamic flow caused by a rotating disk was examined by [3]. Also, [4] analyzed the flow of nanofluid passed an inclined rotating disk, whereas [5] looked at the upshot of convective heat transfer in fluid flow as a result of a rotating disk. As well, the flow of Ag-water-based nanofluid due to a rotating disk in the course of uneven thickness was observed by [6]. In recent times, [7] analyzed CNT-ethylene glycol nanofluid flow caused by a stretchable rotating disk with the Cattaneo-Christov heat flux model. [8] investigated entropy generation, and slip persuades in magnetohydrodynamic flow through a permeable rotating disk. [9] observed the flow of the Maxwell nanofluid

overstretching permeable rotating disk, whereas the flow of mixed convection viscoelastic hybrid nanofluid past a rotating disk was examined by [10]. Some of the latest significant works on fluid flow past a rotating disk are also found in [11–15].

In view of the features of shearing stress, fluids can be categorized into Newtonian and non-Newtonian fluids. The Newtonian fluids are described by shearing stress which is linearly associated with the deformation rate, while in the non-Newtonian fluids, shearing stress is nonlinearly associated with the shearing strain rate. Some fluids such as polymeric suspension, industrial colloid fluids, capillaries in liquid crystals, blood flow in arteries, and dust in air fail to describe the characteristics of the Newtonian fluid [16]. In view of this limitation, a number of non-Newtonian fluid models have been suggested to describe their flow features. Among these non-Newtonian fluid models, micropolar fluid has been very active research for the last few decades due to the various applications in the prescribed theme of engineering and industries. Micropolar fluid is a postponement of randomly oriented particles in a viscous medium that show microscopic effects occurring from the fluid elements' micromotions and local structure. Micropolar fluid can be described by spin inertia, micromotion, and couple stress, and it can hold stress moments and body moments [17]. In this fluid, the particles in the small volume element can spin about the centroid of the volume element. Physically, the micropolar fluid represents some anisotropic fluids and the fluids consisting of bar-like elements such as the flow of liquid crystals, polymeric fluid, colloidal fluids, bodily fluids, paints, and suspension fluids [18, 19].

Micropolar fluid theory and its mathematical modeling were initially introduced and formulated by [20]. Subsequently, [21] implemented boundary layer scaling to investigate the simple micropolar fluid theory near a rigid boundary. [22] extended his theory of micropolar fluid by just taking the effects of heat conduction and heat dissipation. A detailed assessment of micropolar fluids and their numerous uses in the subject of industrial and technology was given by [23]. Nowadays, the theory and its applications of the micropolar fluid have received immense attention from many scientists and researchers. For instance, [24] examined the flow of a micropolar fluid over an accelerated rotating disk. The characteristics of heat and mass transfer micropolar fluid from a curved stretching surface subject to the Lorentz forces were examined by [25]. [26] studied the nonlinear convection flow of a micropolar nanofluid due to a rotating disk with multiple slip flows. Also, the material behavior in the micropolar fluid of the Brownian motion over a stretchable disk with the application of thermophoretic forces was analyzed by [27]. Currently, unsteady micropolar hybrid nanofluid flow past a permeable stretching/shrinking vertical plate was examined by [28], and [29] considered boundary layer flow of micropolar nanofluid towards a permeable stretching sheet in the presence of porous medium with thermal radiation and viscous dissipation.

Magnetohydrodynamic is the theme of fluid flow in electrically conducting fluids with magnetic properties that affect fluid flow characteristics. While a magnetic field incidence in an electrically conducting fluid, a current is induced

and polarizes the fluid. MHD boundary layer flow with heat transfer characteristics is more important in numerous technological processes and has received considerable interest due to its significance in practical applications such as plasma studies, MHD power generator designs, petroleum industries, design for cooling of nuclear reactors, and construction of heat exchangers and on the performance of various systems [30]. The incidence of MHD in an electrically conducting fluid creates an opposing force, through which the motions of fluid particles create resistance, which is termed the Lorentz or drag force. Considerably, the effects of this force enhance because of concentration and fluid temperature reducing the boundary layer separation. As a result, [31] analyzed the flow of mixed convection magneto-hydrodynamic micropolar liquid caused by the nonlinear stretched sheet. [32] investigated entropy generation and consequences of binary chemical reaction on the MHD Darcy-Forchheimer Williamson nanofluid flow over a nonlinearly stretching surface. Three-dimensional MHD viscous flows under the influence of thermal radiation and viscous dissipation were examined by [33]. Also, [34] studied heat and mass transfer of magnetically driven 3rd grade (Cu-TiO<sub>2</sub>/engine oil) nanofluid via a convectively heated surface. Some of the latest significant works on MHD nanofluid flow past different geometry are also found in [35–37].

The phenomenon of heat transfer is very significant because of its several applications in engineering, industrial, and biomedical applications. Fourier was the first scientist who stated the most conquering classical heat flux model in continuum mechanics. The core weakness of this model is the temperature field, and the entire system is directly exaggerated by initial disturbance. To keep away from this unrealistic feature, first, Cattaneo improved Fourier's law by adding thermal relaxation time which tolerates the heat flux and [38] established the efficient heat transfer means by the derivative Cattaneo model, and then, it is called the Cattaneo-Christov heat flux model. Presently, much interest has been shown in the study of the Cattaneo-Christov heat flux model. For example, [39] investigated the Casson nanofluid flow over stretching cylinder with variable thermal conductivity and Cattaneo-Christov heat flux model. The flow between two stretchable rotating disks with the Cattaneo-Christov heat flux model was examined by [40]. Also, [41] analyzed the effect of the Cattaneo-Christov heat flux model on MHD micropolar fluid flow past a nonlinearly inclined stretchable rotating disk. Recently, more inspiring work on thermal performance of nanofluid flow was also reported by [42–48].

The objective of this research is to examine magnetohydrodynamic micropolar nanofluid flow due to stretchable rotating disk with microrotation and non-Fourier's heat and non-Fick's mass flux models under the effects of slip and convective boundary conditions employing the spectral local linearization method (SLLM). The SLLM is rooted in decoupling and linearizing systems of equations via a combination of a univariate linearization method and a spectral collocation discretization. The key aspect of the SLLM algorithm is that the system of equations can be solved successively in a very computationally efficient way after a large coupled system of equations is broken into a sequence of

smaller subsystems. [49] confirmed that as compared with other existing numerical methods, the SLLM is stable, accurate, convergent, and very efficient to solve some large systems of boundary value problems. The novelty of this study is the assessment of microscopic effects occurring from the micropolar fluid elements such as micromotion and couple stress, the effects of thermal and concentration relaxations due to non-Fourier's heat and non-Fick's mass flux, and the effects of radial stretching disk on micropolar fluid flow, heat, and mass transfer. The uniqueness of this study is not only to analyze the effects of these embedded parameters, but also, the numerical method used for the analysis is very recent and easy to develop, yet very accurate and convergent iterative algorithm for working with nonlinear systems of boundary layer flow problems [49, 50]. Consequently, employing SLLM, the results of micropolar fluid velocity, microrotation velocity, temperature and concentration fields, skin friction coefficient, couple stress, local heat, and mass transfer rate are specified and discussed with graphs and tables.

## 2. Mathematical Problem Description

**2.1. Flow Model and Governing Equations.** In this study, a steady, laminar flow of an electrically conducting and incompressible micropolar nanofluid flow over an infinite stretchable rotating disk with angular velocity  $\Omega$  about the  $z$ -axis and radially stretching with stretching rate  $s$  is used as given in Figure 1. Cylindrical-coordinate frame  $(r, \theta, z)$  with velocity components  $(u, v, w)$  and  $(\omega_1, \omega_2, \omega_3)$ , the microrotation components are considered whereas the disk is fixed alongside  $z=0$ . The flow is examined under the action of a magnetic field with strength  $B_0$  which is applied normally to the fluid flow. Also, the effects of velocity slip and convective conditions are taken into consideration. At the wall of the surface, a constant value of temperature, denoted by  $T_s$  and the ambient value of temperature, denoted by  $T_\infty$  are assumed. To alter the temperature of the surface  $T_s$  using convective heat transfer mode, heated fluid under the surface with temperature  $T_f$  is also applied. Due to this, a heat transfer coefficient  $h_f$  is offered, and the entire system of the surface of the rotating disk is heated for  $T_f > T_s$  or cooled for  $T_f < T_s$ . With this assumption, for heat transfer, the convective boundary condition is given by  $k(\partial T/\partial z) = h_f(T_f - T)$  imposed on the surface of the rotating disk. Over the heated wall of the surface, concentration is considered to be  $C = C_s + D(\partial C/\partial z)$ , where  $D$  is the solutal jump factor. Moreover, for heat and mass transfer modes, the Cattaneo-Christov non-Fourier heat and non-Fick mass flux models are considered.

Under these assumptions and in consideration of the standard boundary layer equations, the governing equations (continuity, momentum, microrotation, energy, and concentration) of the micropolar fluid flow past a rotating disk are given as follows (see Ref. [10, 17, 40]):

$$\frac{\partial u}{\partial r} + \frac{\partial w}{\partial z} + \frac{u}{r} = 0, \quad (1)$$

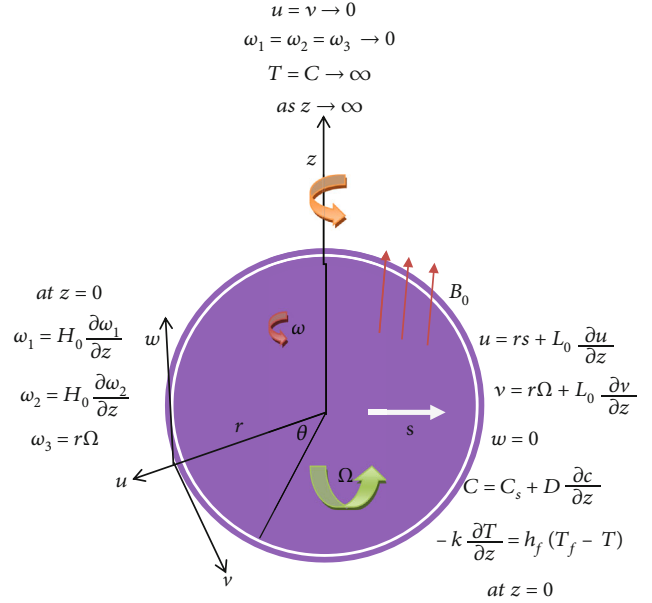


FIGURE 1: Physical flow configuration.

$$u \frac{\partial u}{\partial r} + w \frac{\partial u}{\partial z} - \frac{v^2}{r} = \frac{(\mu + k)}{\rho_f} \left( \frac{\partial^2 u}{\partial r^2} + \frac{1}{r} \frac{\partial u}{\partial r} - \frac{u}{r^2} + \frac{\partial^2 u}{\partial z^2} \right) - \frac{k}{\rho_f} \frac{\partial \omega_2}{\partial z} - \frac{\sigma u B_0^2}{\rho_f}, \quad (2)$$

$$u \frac{\partial v}{\partial r} + w \frac{\partial v}{\partial z} + \frac{uv}{r} = \frac{(\mu + k)}{\rho_f} \left( \frac{\partial^2 v}{\partial r^2} + \frac{1}{r} \frac{\partial v}{\partial r} - \frac{v}{r^2} + \frac{\partial^2 v}{\partial z^2} \right) + \frac{k}{\rho_f} \left( \frac{\partial \omega_1}{\partial z} - \frac{\partial \omega_3}{\partial r} \right) - \frac{\sigma v B_0^2}{\rho_f}, \quad (3)$$

$$u \frac{\partial \omega_1}{\partial r} + w \frac{\partial \omega_1}{\partial z} - \frac{v}{r} \omega_2 = \frac{(\alpha + \beta + \gamma)}{\rho_f j} \frac{\partial}{\partial r} \left( \frac{\partial \omega_1}{\partial r} + \frac{\omega_1}{r} + \frac{\partial \omega_3}{\partial z} \right) - \frac{\gamma}{\rho_f j} \frac{\partial}{\partial z} \left( \frac{\partial \omega_3}{\partial r} - \frac{\partial \omega_1}{\partial z} \right) - \frac{k}{\rho_f j} \frac{\partial v}{\partial z} - \frac{2k}{\rho_f j} \omega_1, \quad (4)$$

$$u \frac{\partial \omega_2}{\partial r} + w \frac{\partial \omega_2}{\partial z} + \frac{v}{r} \omega_1 = \frac{\gamma}{\rho_f j} \left[ \frac{\partial}{\partial r} \left( \frac{\partial \omega_2}{\partial r} + \frac{\omega_2}{r} \right) + \frac{\partial^2 \omega_2}{\partial z^2} \right] + \frac{k}{\rho_f j} \frac{\partial v}{\partial z} - \frac{2k}{\rho_f j} \omega_1, \quad (5)$$

$$u \frac{\partial \omega_3}{\partial r} + w \frac{\partial \omega_3}{\partial z} = \frac{(\alpha + \beta + \gamma)}{\rho_f j} \frac{\partial}{\partial z} \left( \frac{\partial \omega_1}{\partial r} + \frac{\omega_1}{r} + \frac{\partial \omega_3}{\partial z} \right) - \frac{\gamma}{\rho_f j r} \frac{\partial}{\partial r} \left[ r \left( \frac{\partial \omega_1}{\partial z} - \frac{\partial \omega_3}{\partial r} \right) \right] + \frac{k}{\rho_f j} \frac{\partial (rv)}{\partial z} - \frac{2k}{\rho_f j} \omega_3, \quad (6)$$

$$u \frac{\partial T}{\partial r} + w \frac{\partial T}{\partial z} + \lambda_e \Phi_e = \alpha_f \left( \frac{\partial^2 T}{\partial r^2} + \frac{1}{r} \frac{\partial T}{\partial r} + \frac{\partial^2 T}{\partial z^2} \right) - \frac{(\rho c)_p}{(\rho c)_f} D_B \left( \frac{\partial T}{\partial r} \frac{\partial C}{\partial r} + \frac{\partial T}{\partial z} \frac{\partial C}{\partial z} \right) - \frac{(\rho c)_p}{(\rho c)_f} D_B \frac{D_T}{T_\infty} \left[ \left( \frac{\partial T}{\partial r} \right)^2 + \left( \frac{\partial T}{\partial z} \right)^2 \right], \quad (7)$$

$$u \frac{\partial C}{\partial r} + w \frac{\partial C}{\partial z} + \lambda_c \Phi_c = D_B \left( \frac{\partial^2 C}{\partial r^2} + \frac{1}{r} \frac{\partial C}{\partial r} + \frac{\partial^2 C}{\partial z^2} \right) + \frac{D_T}{T_\infty} \left( \frac{\partial^2 T}{\partial r^2} + \frac{1}{r} \frac{\partial T}{\partial r} + \frac{\partial^2 T}{\partial z^2} \right), \quad (8)$$

with associated boundary conditions

$$\begin{aligned} u &= rs + L_0 \frac{\partial u}{\partial z}, \\ v &= r\Omega + L_0 \frac{\partial v}{\partial z}, \\ w &= 0, \\ \omega_1 &= H_0 \frac{\partial \omega_1}{\partial z}, \\ \omega_2 &= H_0 \frac{\partial \omega_2}{\partial z}, \\ \omega_3 &= r\Omega, \\ -k \frac{\partial T}{\partial z} &= h_f (T_f - T), \\ C &= C_s + D \frac{\partial C}{\partial z}, \end{aligned} \quad (9)$$

$$\begin{aligned} \text{at } z &= 0, \\ u &\longrightarrow 0, \\ v &\longrightarrow 0, \\ \omega_1 = \omega_2 = \omega_3 &\longrightarrow 0, \\ T &\longrightarrow T_\infty, \\ C &\longrightarrow C_\infty, \\ \text{as } z &\longrightarrow \infty, \end{aligned} \quad (10)$$

where  $\alpha$ ,  $\beta$ , and  $\gamma$  represent the material constants (angular viscosity coefficients);  $\mu$  is the absolute viscosity;  $\rho_f$ ,  $(\rho c)_f$

and  $(\rho c)_p$  are the density of the fluid, heat capacity of the fluid and heat capacity of nanoparticles, respectively;  $D_B$  and  $D_T$ , respectively, refer to the Brownian and thermophoretic diffusion coefficients;  $j = \chi/\Omega = (\mu + k)/\rho_f \Omega$  is the microinertia per unit mass;  $\sigma$  is electrical conductivity of the fluid;  $k$  is the vortex viscosity (dynamic microrotation viscosity);  $\alpha_f$  is the thermal diffusivity of the fluid;  $\lambda_e$  and  $\lambda_c$ , respectively, refer to the thermal and concentration relaxation time; and  $L_0$  and  $H_0$  stand for momentum slip factor and angular slip factor, respectively. Moreover,  $\Phi_e$  and  $\Phi_c$ , respectively, stand for the Cattaneo-Christove non-Fourier heat and non-Fick mass flux models which are given as follows (see Ref. [7, 40]):

$$\begin{aligned} \Phi_e &= u^2 \frac{\partial^2 T}{\partial r^2} + w^2 \frac{\partial^2 T}{\partial z^2} + 2uw \frac{\partial^2 T}{\partial r \partial z} + \frac{\partial T}{\partial r} \left( u \frac{\partial u}{\partial r} + w \frac{\partial u}{\partial z} \right) \\ &\quad + \frac{\partial T}{\partial z} \left( u \frac{\partial w}{\partial r} + w \frac{\partial w}{\partial z} \right), \\ \Phi_c &= u^2 \frac{\partial^2 C}{\partial r^2} + w^2 \frac{\partial^2 C}{\partial z^2} + 2uw \frac{\partial^2 C}{\partial r \partial z} + \frac{\partial C}{\partial r} \left( u \frac{\partial u}{\partial r} + w \frac{\partial u}{\partial z} \right) \\ &\quad + \frac{\partial C}{\partial z} \left( u \frac{\partial w}{\partial r} + w \frac{\partial w}{\partial z} \right). \end{aligned} \quad (11)$$

**2.2. Similarity Transformation and Transformed Equations.** The above governing equations are highly nonlinear PDEs that are intricate to solve analytically. Thus, to compute numerically, we use the following similarity transformation to transform Equations (1)–(9) into dimensionless nonlinear ODEs (see Ref. [7, 10, 17]):

$$\begin{aligned} \xi &= z \left( \frac{2\Omega}{\chi} \right)^{1/2}, \\ u &= r\Omega f^1(\xi), \end{aligned} \quad (12)$$

$$\begin{aligned} v &= r\Omega g(\xi), \\ w &= -(2\Omega\chi)^{1/2} f(\xi), \end{aligned}$$

$$\begin{aligned} \omega_1 &= r\Omega \left( \frac{2\Omega}{\chi} \right)^{1/2} \psi(\xi), \\ \omega_2 &= r\Omega \left( \frac{2\Omega}{\chi} \right)^{1/2} p(\xi), \\ \omega_3 &= r\Omega q(\xi), \end{aligned} \quad (13)$$

$$\begin{aligned} \theta(\xi) &= \frac{T - T_\infty}{T_f - T_\infty}, \\ \phi(\xi) &= \frac{C - C_\infty}{C_s - C_\infty}, \end{aligned} \quad (14)$$

$$\chi = \frac{\mu + k}{\rho_f},$$

where  $\xi$  is dimensionless similarity variable;  $f(\xi)$  is dimensionless stream function;  $f^l(\xi)$  and  $g(\xi)$  are the dimensionless velocities;  $\psi(\xi)$ ,  $p(\xi)$ , and  $q(\xi)$  are dimensionless microrotations;  $\theta(\xi)$  and  $\phi(\xi)$  are, respectively, dimensionless temperature and concentration of nanofluid.

Utilizing Equation (13), the continuity Equation (1) is identically fulfilled, and the governing Equations (2)–(8) with boundary conditions are altered into the following dimensionless form:

$$2f^{lll} + 2ff^{ll} - f^{l^2} + g^2 - 2A_1p^l - Mf^l = 0, \tag{15}$$

$$2g^{ll} - 2(f^l g - f g^l) + 2A_1\psi^l - Mg = 0, \tag{16}$$

$$2\psi^{ll} - A_2(g^l + 2\psi) - A_3(f^l\psi - 2f\psi^l - gp) = 0, \tag{17}$$

$$2p^{ll} + A_2(f^{ll} - 2p) - A_3(f^l p - 2fp^l + g\psi) = 0, \tag{18}$$

$$2q^{ll} - 4A_4\psi^l - 2A_5(g + q) - A_6(f^l q - 2fq^l) = 0, \tag{19}$$

$$\theta^{ll} + Pr(Nb\phi^l\theta^l + Nt\theta^{l^2} + f\theta^l) - 2\alpha_t Pr(f^2\theta^{ll} + ff^l\theta^l) = 0, \tag{20}$$

$$\phi^{ll} + Scf\phi^l + \frac{Nt}{Nb}\theta^{ll} - 2\alpha_c Sc(f^2\phi^{ll} + ff^l\phi^l) = 0, \tag{21}$$

and corresponding boundary condition Equation (9) takes the form

$$\begin{aligned} f(0) &= 0, \\ f^l(0) &= \Lambda + \delta f^{ll}(0), \\ g(0) &= 1 + \delta g^l(0), \end{aligned} \tag{22}$$

$$\begin{aligned} \psi(0) &= s_0\psi^l(0), \\ p(0) &= s_0p^l(0), \\ q(0) &= 1, \end{aligned} \tag{23}$$

$$\begin{aligned} \theta(0) &= 1 + Bi\theta^l(0), \\ \phi(0) &= 1 + S_i\phi^l(0), \\ \text{at } \xi &= 0, \end{aligned} \tag{24}$$

$$\begin{aligned} f^l &\longrightarrow 0, \\ g &\longrightarrow 0, \\ \psi &\longrightarrow 0, \\ p &\longrightarrow 0, \\ q &\longrightarrow 0, \\ \theta &\longrightarrow 0, \\ \phi &\longrightarrow 0, \\ \text{as } \xi &\longrightarrow \infty, \end{aligned} \tag{25}$$

where prime denotes differential with respect to  $\xi$ ;  $M = \sigma B_0^2 / \rho_f \Omega$  is the magnetic parameter;  $A_1 = k/(k + \mu)$ ,  $A_2 = k\chi/\gamma\Omega$ ,  $A_3 = \rho_f j\chi/\gamma$ ,  $A_4 = (\alpha + \beta)/(\alpha + \beta + \gamma)$ ,  $A_5 = k\chi/(\alpha + \beta + \gamma)\Omega$ , and  $A_6 = \rho_f j\chi/(\alpha + \beta + \gamma)$  are microrotation parameters;  $Nb = ((\rho c)_p/(\rho c)_f)(D_B(C_s - C_\infty)/\chi)$  is the Brownian motion parameter;  $Nt = ((\rho c)_p/(\rho c)_f)(D_T(T_f - T_\infty)/\chi T_\infty)$  is the thermophoresis parameter;  $Pr = \chi/\alpha_f$  is the Prandtl number;  $Le = \alpha_f/D_B$  is the Lewis number;  $Sc = PrLe = \chi/D_B$  is the Schmidt number;  $\alpha_t = \lambda_e\Omega$  is the thermal relaxation parameter;  $\alpha_c = \lambda_c\Omega$  is the concentration relaxation parameter;  $\Lambda = s/\Omega$  is the scaled stretching parameter;  $\delta = L_0(2\Omega/\chi)^{1/2}$  is the velocity slip parameter;  $s_0 = H_0(2\Omega/\chi)^{1/2}$  is the microrotation slip parameter;  $Bi = h_f(2\Omega/\chi)^{1/2}$  is the thermal slip parameter; and  $S_i = D(2\Omega/\chi)^{1/2}$  is the solutal jump parameter.

**2.3. Engineering Quantities of Interest.** The physical quantities of importance in this study are the skin friction coefficient ( $C_{f_r}$ ), couple stress  $C$ , local Nusselt number ( $Nu_r$ ), and local Sherwood number ( $Sh_r$ ), and, respectively, defined as (see Ref. [17, 26])

$$\begin{aligned} C_{f_r} &= 2 \frac{\tau_w}{\rho_f (r\Omega)^2}, \\ C_{s_r} &= \frac{t_{wr}}{\rho_f \chi j \Omega r^2}, \\ C_{s_\theta} &= \frac{t_{w\theta}}{\rho_f \chi j \Omega r^2}, \\ C_{s_z} &= \frac{t_{wz}}{\rho_f \chi j \Omega r^2}, \\ Nu_r &= \frac{rq_w}{k(T_f - T_\infty)}, \\ Sh_r &= \frac{rJ_w}{D_B(C_s - C_\infty)}, \end{aligned} \tag{26}$$

where these parameters describe the local shear stress at the wall ( $\tau_{zr}, \tau_{z\theta}$ ), wall couple stress ( $t_{wr}, t_{w\theta}, t_{wz}$ ), wall heat flux ( $q_w$ ), and wall mass flux ( $J_m$ ) given as (see Ref. [17, 26])

$$\begin{aligned}
\tau_{zr} &= (\mu + k) \left( \frac{\partial u}{\partial z} \right)_{z=0}, \\
\tau_{z\theta} &= (\mu + k) \left( \frac{\partial v}{\partial z} \right)_{z=0}, \\
\tau_w &= (\tau_{zr}^2 + \tau_{z\theta}^2)^{1/2}, \\
t_{wr} &= -(\alpha + \beta + \gamma) \left( \frac{\partial \omega_1}{\partial z} \right)_{z=0}, \\
t_{w\theta} &= \gamma \left( \frac{\partial \omega_2}{\partial z} \right)_{z=0}, \\
t_{wz} &= (\alpha + \beta + \gamma) \left( \frac{\partial \omega_3}{\partial z} \right)_{z=0}, \\
q_w &= -k \left( \frac{\partial T}{\partial z} \right)_{z=0}, \\
J_m &= -D_B \left( \frac{\partial C}{\partial z} \right)_{z=0}.
\end{aligned} \tag{27}$$

Consequently, the dimensionless skin friction coefficient, couple stress coefficient, local Nusselt number, and local Sherwood number are, respectively, given by

$$\begin{aligned}
(\text{Re}_r)^{1/2} C_f &= 2(1+K) \left( f^{\parallel}(0)^2 + g^{\parallel}(0)^2 \right)^{1/2}, \\
\frac{A_3 C_{sr}}{\text{Re}_r} &= 2\psi^{\parallel}(0), \\
\frac{A_6 C_{s\theta}}{\text{Re}_r} &= -2p^{\parallel}(0), \\
A_6 C_{sz} \left( \frac{\chi}{2\Omega} \right)^{1/2} &= -q^{\parallel}(0), \\
Nu_r (\text{Re}_r)^{-1/2} &= -\theta^{\parallel}(0), \\
Sh_r (\text{Re}_r)^{-1/2} &= -\phi^{\parallel}(0),
\end{aligned} \tag{28}$$

where  $K = k/\mu$  is the material parameter and  $\text{Re}_r$  is the local Reynolds number defined by  $\text{Re}_r = (r\Omega)r/\chi$ .

### 3. Numerical Method of Solution

The systems of coupled ODEs in Equations (15)–(21) are nonlinear and intricate to solve analytically. Thus, to compute such large coupled systems, numerical methods should be utilized. Owing to this, we employ a numerically simple, yet accurate, convergent, stable, and very efficient method known as the spectral local linearization method (SLLM) [49]. The SLLM is rooted in a decoupling and linearization system of equations employing a blend of a univariate linearization and a spectral collocation concretization. A full description of the development of SLLM for the systems of the nonlinear ordinary differential equation was given by [49]. To use the proposed SLLM iterative method, first, it is suitable to reduce the order of the governing Equation (15) by one setting  $f^{\parallel}(\xi) = h(\xi)$ ; then, considering that  $f(\xi)$

and  $h(\xi)$  are known at each iteration level, the local linearization iteration algorithm can be articulated as

$$2h_{r+1}^{\parallel} + 2f_r h_{r+1}^{\parallel} - 2h_r h_{r+1} - Mh_{r+1} = h_r^2 - g_r^2 + 2A_1 p_r^{\parallel}, \tag{29}$$

$$2g_{r+1}^{\parallel} + 2f_r g_{r+1}^{\parallel} - 2h_{r+1} g_{r+1} - M g_{r+1} = -2A_1 \psi_r^{\parallel}, \tag{30}$$

$$2\psi_{r+1}^{\parallel} - 2A_2 \psi_{r+1} - A_3 h_{r+1} \psi_{r+1} + 2A_3 f_r \psi_{r+1}^{\parallel} = A_2 g_{r+1}^{\parallel} - A_3 p_r g_{r+1}, \tag{31}$$

$$2p_{r+1}^{\parallel} + 2A_2 p_{r+1} - A_3 h_{r+1} p_{r+1} + 2A_3 f_r p_{r+1}^{\parallel} = -A_2 h_{r+1}^{\parallel} + A_3 g_{r+1} \psi_{r+1}, \tag{32}$$

$$2q_{r+1}^{\parallel} - 2A_5 q_{r+1} - A_6 h_{r+1} q_{r+1} + 2A_6 f_r q_{r+1}^{\parallel} = 4A_4 \psi_{r+1}^{\parallel} + 2A_5 g_{r+1}, \tag{33}$$

$$\begin{aligned}
\frac{1}{\text{Pr}} \theta_{r+1}^{\parallel} + (Nb\phi_r^{\parallel} + 2Nt\theta_r^{\parallel} + f_r) \theta_{r+1}^{\parallel} \\
- 2\alpha_t (f_r^2 \theta_{r+1}^{\parallel} + f_r h_{r+1} \theta_{r+1}^{\parallel}) = Nt (\theta_r^{\parallel})^2,
\end{aligned} \tag{34}$$

$$\frac{1}{\text{Sc}} \phi_{r+1}^{\parallel} + f_r \phi_{r+1}^{\parallel} - 2\alpha_c (f_r^2 \phi_{r+1}^{\parallel} + f_r h_{r+1} \phi_{r+1}^{\parallel}) = \frac{Nt}{Nb} \theta_{r+1}^{\parallel}, \tag{35}$$

$$\begin{aligned}
f_{r+1}^{\parallel} &= h_{r+1}, \\
f_{r+1}^{\parallel}(0) &= 0,
\end{aligned} \tag{36}$$

subject to boundary condition

$$\begin{aligned}
h_{r+1}(0) &= \Lambda + \delta h_{r+1}^{\parallel}(0), \\
g_{r+1}(0) &= 1 + \delta g_{r+1}^{\parallel}(0),
\end{aligned} \tag{37}$$

$$\begin{aligned}
h_{r+1}(\infty) &= 0, \\
g_{r+1}(\infty) &= 0,
\end{aligned} \tag{38}$$

$$\begin{aligned}
\psi_{r+1}(0) &= s_0 \psi_{r+1}^{\parallel}(0), \\
p_{r+1}(0) &= s_0 p_{r+1}^{\parallel}(0),
\end{aligned} \tag{39}$$

$$\begin{aligned}
q_{r+1}(0) &= 1, \\
\psi_{r+1}(\infty) &= 0, \\
p_{r+1}(\infty) &= 0, \\
q_{r+1}(\infty) &= 0,
\end{aligned} \tag{40}$$

$$\theta_{r+1}(0) = 1 + Bi\theta_{r+1}^{\parallel}(0), \tag{41}$$

$$\begin{aligned}
\phi_{r+1}(0) &= 1 + S_i \phi_{r+1}^{\parallel}(0), \\
\theta_{r+1}(\infty) &= 0, \\
\phi_{r+1}(\infty) &= 0,
\end{aligned} \tag{42}$$

where the terms  $r + 1$  and  $r$  represent the current and previous iteration levels, respectively.

Equations (29)–(36) with boundary conditions Equation (39) are computed using the Chebyshev pseudospectral

TABLE 1: SLLM solution convergence test.

Iter. order	$(Re_r)^{1/2}C_f$	$(Re_r)^{1/2}C_{sr}$	$(Re_r)^{-1/2}Nu_r$	$(Re_r)^{-1/2}Sh_r$
01	5.45024509	-6.68503429	0.23819532	0.29649267
02	8.84266291	-7.36652464	0.57204639	0.47266923
03	8.61607846	-7.38124266	0.45346969	0.42615330
04	8.65488503	-7.38047576	0.47199029	0.43281214
05	8.64862301	-7.38055477	0.46993727	0.43198037
06	8.64966278	-7.38054245	0.47031524	0.43212847
07	8.64948823	-7.38054443	0.47024534	0.43210260
08	8.64951765	-7.38054410	0.47025485	0.43210639
09	8.64951268	-7.38054416	0.47025316	0.43210572
10	8.64951352	-7.38054415	0.47025348	0.43210584
11	8.64951338	-7.38054415	0.47025344	0.43210582
12	8.64951340	-7.38054415	0.47025344	0.43210583
13	8.64951340	-7.38054415	0.47025344	0.43210583
14	8.64951340	-7.38054415	0.47025344	0.43210583

TABLE 2: Grid-independence test for SLLM solutions.

Iter. order	$N$	$(Re_r)^{1/2}C_f$	$(Re_r)^{1/2}C_{sr}$	$(Re_r)^{-1/2}Nu_r$	$(Re_r)^{-1/2}Sh_r$
12	10	8.66080368	-7.38054868	0.47024587	0.43210351
12	20	8.64951339	-7.38054415	0.47025344	0.43210583
12	30	8.64951340	-7.38054415	0.47025344	0.43210583
12	50	8.64951340	-7.38054415	0.47025344	0.43210583
12	100	8.64951340	-7.38054415	0.47025344	0.43210583
12	150	8.64951340	-7.38054415	0.47025344	0.43210583
12	200	8.64951340	-7.38054415	0.47025344	0.43210583

TABLE 3: Confirmation results of  $-\theta(0)$  for the values of the Biot number  $Bi$  with  $Pr = 0.72, Nb = Sc = 1$ , and values of the rest parameter zero.

$Bi$	[10]	[51]	[52]	Current upshot
0.05	0.144661	0.144661	0.144661	0.14466131
0.1	0.252758	0.252758	0.252758	0.25275796
0.2	0.403523	0.403523	0.403522	0.40352274
0.4	0.575014	0.575014	0.575013	0.57501363
0.6	0.669915	0.669916	0.669915	0.66991582
0.8	0.730170	0.730170	0.730169	0.73017015
1.0	0.771822	0.771822	0.771822	0.77182232
5.0	0.944174	0.944174	0.944173	0.94417371
10.0	0.971285	0.971285	0.971285	0.97128494

method. The unknown functions are given by the Chebyshev interpolating polynomials with the Gauss-Lobatto points as (see Ref. [53, 54])

$$x_m = \cos\left(\frac{m\pi}{N}\right), m = 0, 1, 2, \dots, N, -1 \leq x_m \leq 1, \quad (43)$$

where  $N$  is the number of collocation points.

The semi-infinite interval  $[0, l_\infty)$  is converted into  $[-1, 1]$  using the linear transformation  $\xi = (l_\infty/2)(x_m + 1)$ , where  $l_\infty$  is large, yet a finite number is chosen to indicate the behavior of the flow features of the boundary condition value at infinity. Chebyshev differentiation matrix is applied to approximate the derivatives of the unknown functions (for details, refer [53]). Starting with suitable initial approximations, the iteration schemes are used iteratively to get the unknown functions at  $r + 1$  iteration levels. Finally, the

system of Equations (29)–(36) can be solved as matrix phase by phase as

$$\begin{aligned}
M_1 H_{r+1} &= B_{1,r}, h_{r+1}(x_N) - \delta h_{r+1}^l(x_N) = \Lambda, h_{r+1}(x_0) = 0, \\
M_2 G_{r+1} &= B_{2,r}, g_{r+1}(x_N) - \delta g_{r+1}^l(x_N) = 1, g_{r+1}(x_0) = 0, \\
M_3 \Psi_{r+1} &= B_{3,r}, \psi_{r+1}(x_N) - s_0 \psi_{r+1}^l(x_N) = 0, \psi_{r+1}(x_0) = 0, \\
M_4 P_{r+1} &= B_{4,r}, p_{r+1}(x_N) - s_0 p_{r+1}^l(x_N) = 0, p_{r+1}(x_0) = 0, \\
M_5 Q_{r+1} &= B_{5,r}, q_{r+1}(x_N) = 1, q_{r+1}(x_0) = 0, \\
M_6 \Theta_{r+1} &= B_{6,r}, \theta_{r+1}(x_N) - Bi \theta_{r+1}^l(x_N) = 1, \theta_{r+1}(x_0) = 0, \\
M_7 \Phi_{r+1} &= B_{7,r}, \phi_{r+1}(x_N) - S_i \phi_{r+1}^l(x_N) = 1, \phi_{r+1}(x_0) = 0, \\
Df_{r+1} &= h_{r+1}, \\
f_{r+1}(x_N) &= 0,
\end{aligned} \tag{44}$$

where

$$\begin{aligned}
M_1 &= 2D^2 + 2[f_r]_d D - 2[h_r]_d - MI, B_{1,r} = h_r^2 - g_r^2 + 2A_1 p_r^l, \\
M_2 &= 2D^2 + 2[f_r]_d D - 2[h_{r+1}]_d - MI, B_{2,r} = -2A_1 \psi_r^l, \\
M_3 &= 2D^2 + 2A_3[f_r]_d D - A_3[h_{r+1}]_d - 2A_2 I, B_{3,r} = A_2 g_{r+1}^l \\
&\quad - A_3 p_r g_{r+1}, \\
M_4 &= 2D^2 + 2A_3[f_r]_d D - A_3[h_{r+1}]_d + 2A_2 I, B_{4,r} = -A_2 h_{r+1}^l \\
&\quad + A_3 g_{r+1} \psi_{r+1}, \\
M_5 &= 2D^2 + 2A_6[f_r]_d D - A_6[h_{r+1}]_d - 2A_5 I, B_{5,r} = 4A_4 \psi_{r+1}^l \\
&\quad + 2A_5 g_{r+1}, \\
M_6 &= \left( \frac{1}{Pr} I - 2\alpha_t [f_r^2]_d \right) D^2 + (Nb[\phi_r]_d + 2Nt[\theta_r]_d \\
&\quad + [f_r]_d - 2\alpha_t [f_r]_d [h_{r+1}]_d) D, B_{6,r} = Nt\theta_r^l, \\
M_7 &= \left( \frac{1}{Sc} I - 2\alpha_c [f_r^2]_d \right) D^2 + ([f_r]_d - 2\alpha_c [f_r]_d [h_{r+1}]_d) D, B_{7,r} \\
&= \frac{Nt}{Nb\theta_r^l}.
\end{aligned} \tag{45}$$

$H_{r+1} = [h_{r+1,0}, h_{r+1,1}, \dots, h_{r+1,N}]^t$ ,  $G_{r+1} = [g_{r+1,0}, g_{r+1,1}, \dots, g_{r+1,N}]^t$ ,  $\Psi_{r+1} = [\psi_{r+1,0}, \psi_{r+1,1}, \dots, \psi_{r+1,N}]^t$ ,  $P_{r+1} = [p_{r+1,0}, p_{r+1,1}, \dots, p_{r+1,N}]^t$ ,  $Q_{r+1} = [q_{r+1,0}, q_{r+1,1}, \dots, q_{r+1,N}]^t$ ,  $\Theta_{r+1} = [\theta_{r+1,0}, \theta_{r+1,1}, \dots, \theta_{r+1,N}]^t$ ,  $\Phi_{r+1} = [\phi_{r+1,0}, \phi_{r+1,1}, \dots, \phi_{r+1,N}]^t$ , and  $F_{r+1} = [f_{r+1,0}, f_{r+1,1}, \dots, f_{r+1,N}]^t$  are column vectors of size  $(N+1)1$ ,  $[\dots]_d$ , and  $I$ , respectively, represents a diagonal

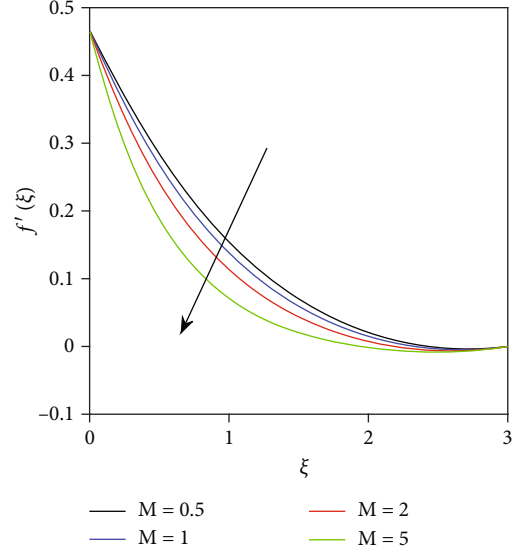


FIGURE 2: Radial velocity profiles for magnetic field parameter  $M$ .

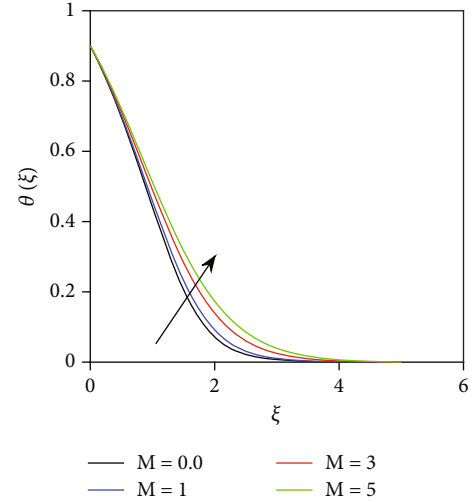


FIGURE 3: Temperature profiles for magnetic field parameter  $M$ .

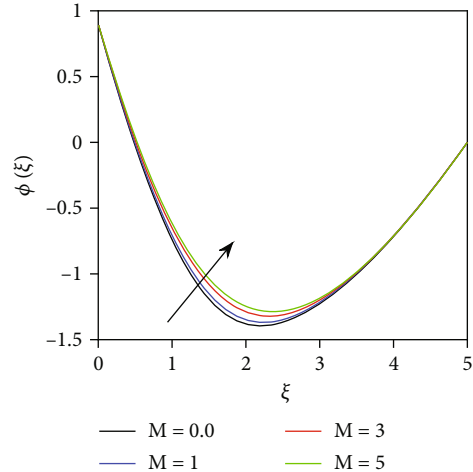


FIGURE 4: Concentration profiles for magnetic field parameter  $M$ .

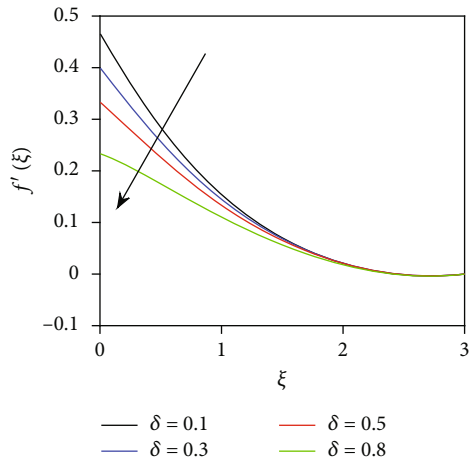


FIGURE 5: Radial velocity profiles for velocity slip parameter  $\delta$ .

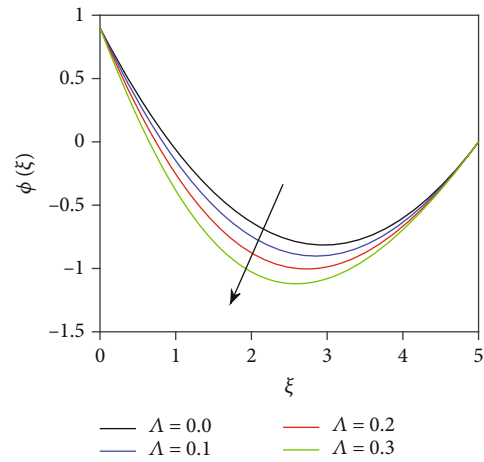


FIGURE 8: Concentration profiles for scaled stretching parameter  $\Lambda$ .

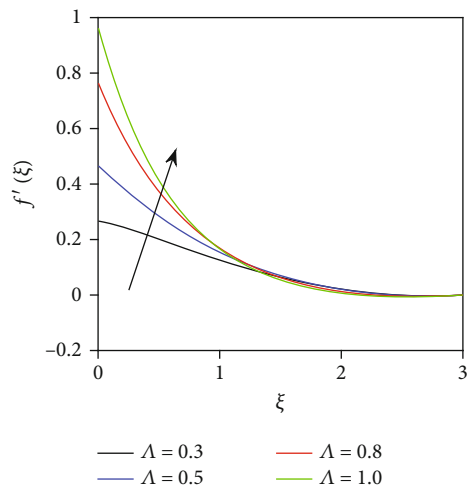


FIGURE 6: Radial velocity profiles for scaled stretching parameter  $\Lambda$ .

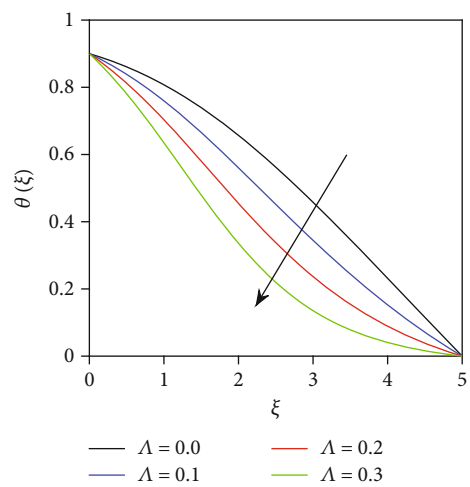


FIGURE 7: Temperature profiles for scaled stretching parameter  $\Lambda$ .

TABLE 4: Four cases for values of micropolar material constants.

Cases	$A_1$	$A_2$	$A_3$	$A_4$	$A_5$	$A_6$
I	0.1	0.1	0.2	0.3	0.2	0.3
II	0.2	0.2	0.3	0.5	0.3	0.5
III	0.3	0.3	0.4	0.6	0.4	0.6
IV	0.4	0.4	0.5	0.8	0.5	0.8

matrix and identity matrix of size  $(N + 1) \times (N + 1)$ . Beginning with the suitable initial approximations given below, the iteration schemes are use diteratively to find  $f_{r+1}, h_{r+1}, g_{r+1}, \psi_{r+1}, p_{r+1}, q_{r+1}, \theta_{r+1}$  and  $\phi_{r+1}$  for  $r = 0, 1, 2, \dots$  (refer [39])

$$\begin{aligned}
 f_0(\xi) &= \frac{\Lambda(1 - e^{-\xi})}{1 + \delta}, \\
 g_0(\xi) &= \frac{e^{-\xi}}{1 + \delta}, \\
 \psi_0(\xi) &= e^{-\xi/s_0}, \\
 p_0(\xi) &= e^{-\xi/s_0}, \\
 q_0(\xi) &= e^{-\xi}, \\
 \theta_0(\xi) &= \frac{e^{-\xi}}{1 + Bi}, \\
 \phi_0(\xi) &= \frac{e^{-\xi}}{1 + S_i}.
 \end{aligned}
 \tag{46}$$

### 4. Results and Discussions

In this section, the numerical outcomes for the large systems of nonlinear ordinary differential equations specified in Equations (15)–(21) with boundary stipulations Equation (24) are computed numerically for various values of more noticeable governing parameters via the efficient method called spectral local linearization method (SLLM), and the upshots are provided by means of tables and graphical

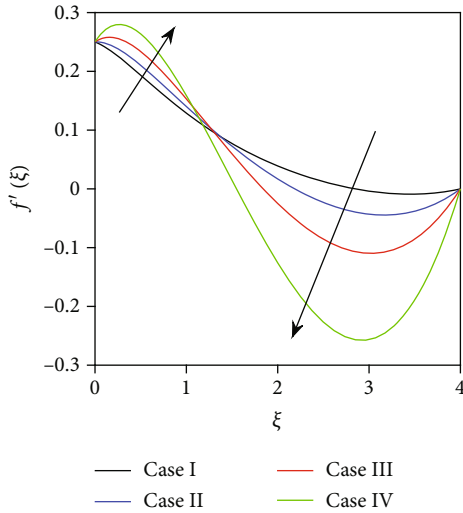


FIGURE 9: Radial velocity profiles for micropolar material constants  $A_1 - A_6$ .

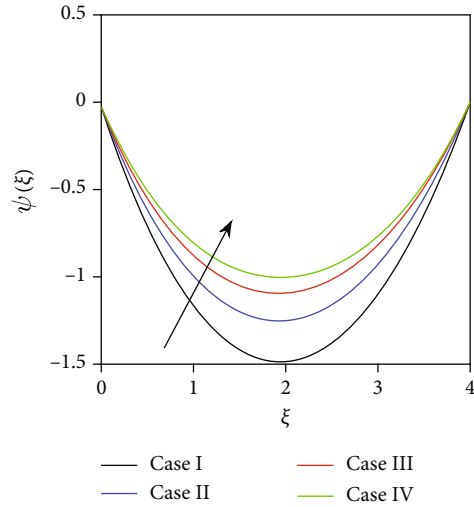


FIGURE 11: Microrotation  $\psi(\xi)$  profiles for micropolar material constants  $A_1 - A_6$ .

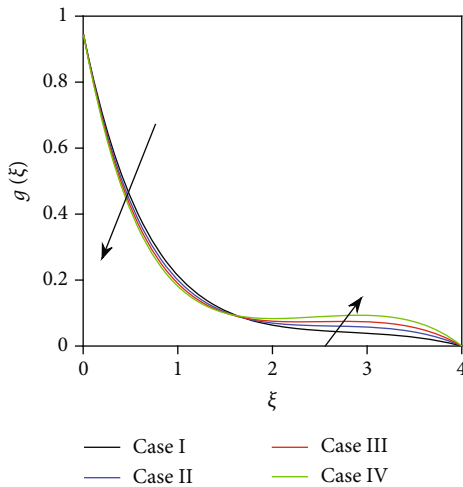


FIGURE 10: Tangential velocity profiles for micropolar material constants  $A_1 - A_6$ .

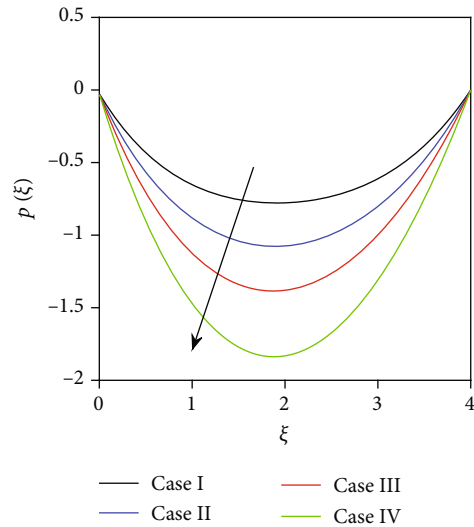


FIGURE 12: Microrotation  $p(\xi)$  profiles for micropolar material constants  $A_1 - A_6$ .

depiction. For the entire output, unless it is specified, SLLM results presented in existing work are obtained with the default values of the ensuing parameters  $M = 0.5, A_1 = 0.1, A_2 = 0.3, A_3 = 0.3, A_4 = 0.2, A_5 = 0.2, A_6 = 0.3, Nb = 0.2, Nt = 0.1, Pr = 1.6, \Lambda = 0.2, \alpha_t = 0.2, \alpha_c = 0.2, \delta = 0.1, s_0 = 0.1, Bi = 0.5, Si = 0.5, Sc = 0.5, K = 0.1$ , and with node  $N = 50$ .

The convergence scrutiny is conceded for skin friction coefficients, couple stress, and local Nusselt and Sherwood numbers, and it is evident that the 12<sup>th</sup> order of approximation is adequate for these physical quantities, as revealed in Table 1. Also, the accuracy of the SLLM is tartan by means of the grid-invariance test at the 12<sup>th</sup> order iteration selecting mesh with nodes  $N = 10, 20, 30, 50, 100, 150$ , and 200 for the skin friction coefficients, couple stress, and local Nusselt and Sherwood numbers, as presented in Table 2. Noticeably, the accuracy is not pretentious up to eight decimal points when mounting the number of nodes to more than  $N = 30$ , except

it merely augments the compilation time. Moreover, the result of the local Nusselt number is matched up with the formerly available results reported in references [10, 51, 52] for similar parameters, and it offers a dreadfully good agreement, as reported in Table 3. Thus, the employed numerical scheme (SLLM) is stable, accurate, and fast converged, and we are very confident in using it.

The effect of magnetic field parameter  $M$  on radial velocity profile is reported in Figure 2. It is revealed that the radial velocity profile is notably reduced with a growth of  $M$ . It is noticeable that the magnetic field robustly depends on the Lorentz force, which is stronger for a larger magnetic field and the lesser magnetic field allied with the weaker Lorentz force. Consequently, intensification in the values of magnetic field parameter, the radial velocity profile, and its boundary

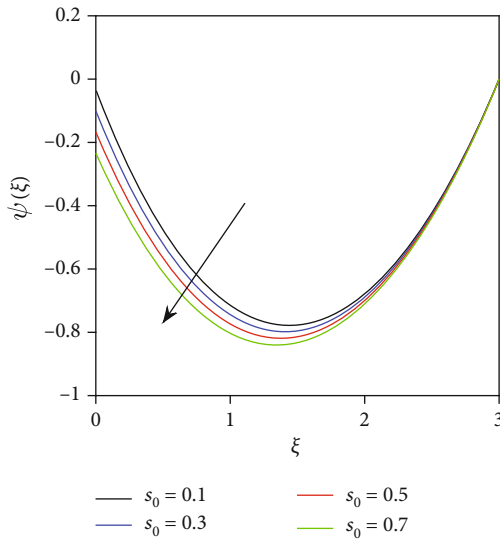


FIGURE 13: Microrotation  $\psi(\xi)$  profiles for microrotation slip parameter  $s_0$ .

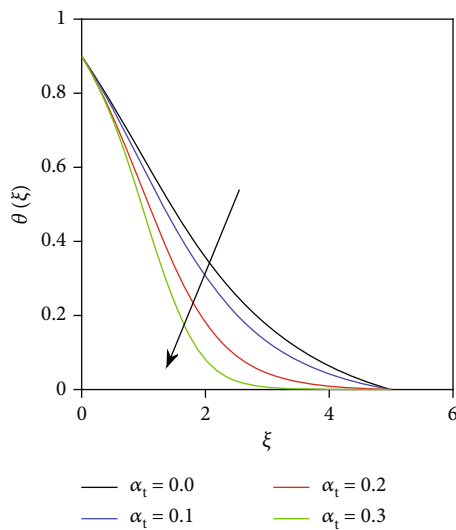


FIGURE 14: Temperature profiles for thermal relaxation parameter  $\alpha_t$ .

layer thickness is considerably turned down. The temperature profile  $\theta(\xi)$  ascends as values of  $M$  ascends, as reported in Figure 3. This is inconsequence of the fact that growth in the values of magnetic field parameters in the flow surface area entails growth up the Lorentz force in the boundary layer flow which generates the Lorentz heating in the energy equation, which is used as the additional heat source to the flow system. Also, Figure 4 exhibits the effects of magnetic field parameter  $M$  on concentration profile  $\phi(\xi)$ . It is observed that the concentration profile with its concentration boundary layer thickness goes up with enlarging values of  $M$ .

The impact of slip parameter  $\delta$  on radial velocity profile is demonstrated in Figure 5. It points up that the radial velocity profile  $f'(\xi)$  is diminution with mounting values

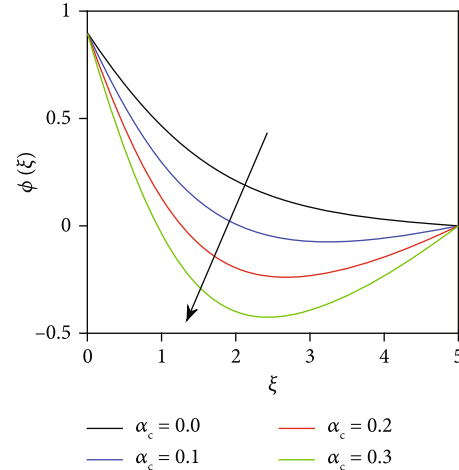


FIGURE 15: Concentration profiles for concentration relaxation parameter  $\alpha_c$ .

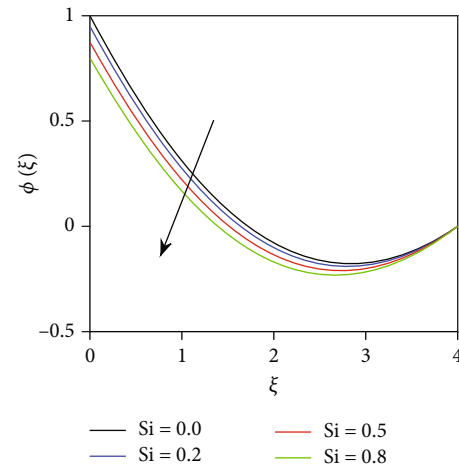


FIGURE 16: Concentration profiles for solutal jump parameter  $Si$ .

of  $\delta$ . Likewise, the velocity boundary thickness is thinning as the value of  $\delta$  is getting higher. The rationale is that the rotating disk as a result of centrifugal force throws the fluid particles outward attached to it. As slip grows, a reduced amount of fluid particles will stick to the disk, and as a result, the small circumferential momentum of the rotating disk moves to the fluid, and finally, small fluid streams subsist in the axial direction. Figures 6–8, respectively, illustrate the radial velocity, temperature, and concentration profiles for the altered value of scaled stretching parameter  $\Lambda$ , which is set as  $\Lambda = s/\Omega$  and measures a radial stretching rate. Figure 6 reveals that the radial velocity grows and momentum boundary layer grow to be thicker with higher values of  $\Lambda$ . In fact, the radial stretching rate gets higher as the value of  $\Lambda$  improves which accelerates the radially superficial flow. It is also observed that temperature and concentration profiles turn down, and the thermal and concentration boundary layers become thinner as the value of  $\Lambda$  improves, as revealed in Figures 7 and 8. Thus, in realistic uses, radial stretching of the disk is obliging to advance the cooling process of the rotating disk.

TABLE 5: Values of the normalized skin friction coefficient and wall couple stress for  $Nb = 0.2$ ,  $Nt = 0.1$ ,  $Pr = 1.6$ ,  $\alpha_t = 0.2$ ,  $\alpha_c = 0.2$ ,  $Bi = 0.5$ ,  $Si = 0.5$ ,  $Sc = 0.5$ , and  $K = 0.1$  with node  $N = 50$ .

$M$	$\delta$	$\Lambda$	$A_1 - A_6$	$S_0$	$(Re_r)^{1/2} C_f$	$(Re_r)^{1/2} C_{sr}$	$(Re_r)^{1/2} C_{s\theta}$
0.5	0.1	0.2	II	0.1	3.52812895	-7.77478860	4.82380334
1					4.26182790	-7.75998650	4.81678456
3					7.21312005	-7.71111938	4.79016347
5					10.15956843	-7.67629662	4.76872495
0.5	0.1				3.52812895	-7.77478860	4.82380334
	0.3				2.50260723	-7.73778859	4.75059201
	0.5				1.73061340	-7.70157658	4.67884097
	0.8				0.94909463	-7.64985403	4.57516154
	0.1	0.0			1.76958885	-7.62129441	4.68020183
		0.1			2.51494075	-7.69482882	4.74924844
		0.2			3.52812895	-7.77478860	4.82380334
		0.3			4.86860980	-7.85965865	4.90264485
		0.2	I		3.55641082	-12.93000757	7.14120336
			II		3.52812895	-7.77478860	4.82380334
			III		3.39785333	-5.30985390	4.47662093
			IV		3.18083579	-3.89965639	3.71936077
			II	0.1	3.52812895	-7.77478860	4.82380334
				0.3	3.52956845	-7.49913887	4.62076992
				0.5	3.53103558	-7.22399189	4.41788181
				0.7	3.53328895	-6.81222030	4.11382362

In order to scrutinize the effects of microrotation parameters ( $A_1 - A_6$ ), four different cases are considered by choosing subjectively as specified in Table 4. Figure 9 discloses that enhancement in values of microrotation parameters ( $A_1 - A_6$ ) results in enlargement of the extent of radial velocity profiles close to the surface of the disk, but it declines with enrichment of microrotation parameters outlying from the surface. Also, Figure 10 reveals the reverse manners observed for tangential velocity profiles with an increase in microrotation parameters. This points out that the occurrence of microrotation viscosity will decline the radial velocity, and the kinetic energy of the fluid is reduced to some extent far away from the surface. The effects of microrotation parameters ( $A_1 - A_6$ ) on microrotation velocities are noticeable in Figures 11 and 12. The outcomes confirm that the absolute value of radial microrotation velocity improves while the absolute value of tangential microrotation velocity reduces with the growth in microrotation parameters. Physically, the augment in angular viscosity coefficients obstructs the incidence of microrotation and weakens the creation of fluid vortices, leading to the steady development of normal fluids into micropolar fluids. On the whole, as microrotation parameters are the ratio of the microrotation viscosity and the angular viscosity coefficients, the angular viscosity coefficient is a constraint to microrotation velocity while the translational velocity is restricted by the microrotation viscosity. Also, from Figure 13, it is illustrated that growth in the values of microrotation slip parameter  $S_0$  in boundary layer flow region tends to trim down the angular velocity profile.

Enrichment in the value of thermal relaxation parameter ( $\alpha_t$ ) illustrates diminish in temperature profile and thermal boundary layer thickness, as reported in Figure 14. To be precise, an enhancement in the thermal relaxation parameter causes a reduced amount of heat to be conveyed from the surface of the disk to the fluid. Thus, the heat conveys swiftly throughout the material, and temperature distribution is elevated for  $\alpha_t = 0$ . Explicitly, the temperature distribution for classical Fourier's law of heat conduction is more than that of the Cattaneo-Christov heat flux model. Also, an improvement in the value of the concentration relaxation parameter ( $\alpha_c$ ) shows diminishes in behavior for concentration profile and its boundary layer thickness, as illustrated in Figure 15. Explicitly, a raise in concentration relaxation parameter results in lower mass diffusivity, and it produces a thinner concentration boundary layer. The effect of solutal jump parameter  $Si$  on concentration profiles is shown in Figure 16. Here, the concentration profile declines as the values of solutal jump parameter develop in the region of the boundary layer. Effects take place as a result of the decline in the kinematic viscosity of the fluid which turns down mass diffusivity that leads to a reduction in concentration boundary layer thicknesses.

The impact of magnetic field parameter  $M$ , scaled stretching parameter  $\Lambda$ , velocity slip parameter  $\delta$ , microrotation parameters ( $A_1 - A_6$ ), and microrotation slip parameters  $S_0$  on normalized skin friction coefficient and wall couple stress are exhibited in Table 5. It observed that normalized skin friction coefficient improves with an escalation

TABLE 6: Values of local heat and mass transfer rate for  $Pr = 1.6$ ,  $\alpha_t = 0.2$ ,  $\alpha_c = 0.2$ ,  $\delta = 0.1$ ,  $S_0 = 0.1$ ,  $Sc = 0.5$ , and  $K = 0.1$  with node  $N = 50$ .

$M$	$Nb$	$\Lambda$	$A_1 - A_6$	$Nt$	$Bi$	$Si$	$(Re_r)^{-1/2}Nu_r$	$(Re_r)^{-1/2}Sh_r$
0.5	0.2	0.2	II	0.1	0.5	0.5	0.24730816	0.69833546
1							0.24482904	0.69633666
3							0.23855381	0.69129087
5							0.23499338	0.68841794
0.5	0.05						0.27464256	1.88002259
	0.1						0.26531973	1.09212635
	0.2						0.24730816	0.69833546
	0.4						0.21381415	0.50175427
	0.2	0.0					0.16250102	0.62068692
		0.1					0.20395466	0.65775326
		0.2					0.24730816	0.69833546
		0.3					0.29602324	0.74455639
		0.2	I				0.24617986	0.69727626
			II				0.24730816	0.69833546
			III				0.24859726	0.69957414
			IV				0.24997220	0.70094741
			II	0.0			0.35778743	0.31397301
				0.1			0.24730816	0.69833546
				0.2			0.16863813	1.04145249
				0.3			0.11360066	1.36111249
				0.1	0.0		0.29273734	0.69577896
					0.3		0.26563101	0.6973528
					0.5		0.24730816	0.69833546
					0.8		0.21943871	0.69970782
					0.5	0.0	0.24034012	0.75930311
						0.3	0.24450474	0.7227185
						0.5	0.24730816	0.69833546
						0.8	0.25155384	0.66177098

of the values of the magnetic field, scaled stretching, and microrotation slip parameters, while it reduces with more values of velocity slip and microrotation slip parameters. Also, it revealed that both wall couple stresses steadily diminish in absolute value with more values of the magnetic field, velocity slip, microrotation material, and microrotation slip parameters and both growth with a higher value of scaled stretching parameter. Table 6 reports that both the local heat and mass transfer reduce with added values of the magnetic field and Brownian motion parameters while both of them are steadily mounting with higher values of scaled stretching and microrotation parameters. As well, the local heat transfer rate and mass transfer rate, respectively, develop with more values of thermal slip parameter and solutal jump parameter.

### 5. Conclusions

In this study, the problem of magnetohydrodynamic micropolar nanofluid flow due to radially stretching rotating disk with the Cattaneo-Christov non-Fourier heat and non-Fick mass flux model has been inspected. The governing problem

of PDEs is transformed into dimensionless nonlinear ordinary differential equations via suitable similarity alterations and solved computationally by means of the spectral local linearization method (SLLM). It is confirmed that the SLLM is a stable, accurate, convergent, and computationally very efficient way to solve large coupled systems of equations. The consequences of more noticeable embedded parameters on micropolar fluid velocity, microrotation velocity, and temperature and concentration fields are graphically scrutinized and discussed thoroughly. Also, the normalized skin friction coefficient, wall couple stress, local heat, and mass transfer rate were computed and presented in tabular form. In general, main surveillance that has been consequent from the study is concluded as follows:

The radial and tangential velocity profiles and their boundary layer thickness are noticeably turned down while the temperature and concentration profiles with their boundary layer thickness build up with enlarging values of magnetic field parameter  $M$ .

- (i) The radial velocity grows with higher values of radially stretching parameter  $\Lambda$  while the tangential

velocity, temperature, and concentration profiles turn down as the value of  $\Lambda$  improves. Thus, in practical uses, radial stretching of the disk is helpful to advance the cooling process of the rotating disk

- (ii) The occurrence of microrotation viscosity in microrotation parameters ( $A_1 - A_6$ ) declines the radial velocity profile, and the kinetic energy of the fluid is reduced to some extent far away from the surface
- (iii) The augment in angular viscosity coefficients in microrotation parameters ( $A_1 - A_6$ ) obstructs the incidence of microrotation and weakens the creation of fluid vortices, leading to the steady development of normal fluids into micropolar fluids
- (iv) An enhancement in the thermal relaxation parameter  $\alpha_t$  causes a reduced amount of heat to be conveyed from the surface of the disk to the fluid. Thus, the temperature distribution for classical Fourier's law of heat conduction is more as compared to that of the Cattaneo-Christov heat flux model
- (v) The concentration profile declines as the values of the solutal jump parameter  $Si$  develop in the region of the boundary layer, and this effect takes place as a result of the decline in the kinematic viscosity of the fluid which turns down mass diffusivity that leads to a reduction in concentration boundary layer thicknesses

## Nomenclature

$A_1 - A_6$ :	Microrotation parameters
$B_0$ :	Magnetic field of uniform strength
$C_s$ :	Concentration of the surface
$C_f$ :	Local skin friction coefficient
$C$ :	Couple stress
$Bi$ :	Biot number
$D$ :	Solutal jump factor
$D_B$ :	Brownian diffusion coefficients
$D_T$ :	Thermophoretic diffusion coefficients
$f$ :	Dimensionless stream function
$h, g$ :	Dimensionless velocities
$H_0$ :	Angular slip factor
$J_m$ :	Wall mass flux
$k$ :	Dynamic microrotation viscosity
$L_0$ :	Momentum slip factor
$Le$ :	Lewis number
$M$ :	Magnetic field parameter
$Nb$ :	Brownian motion parameter
$Nt$ :	Thermophoresis parameter
$Nu_r$ :	Local Nusselt number
$s_0$ :	Microrotation slip parameter
$S_i$ :	Solutal jump parameter
$Sh_r$ :	Local Sherwood number
$p, q$ :	Dimensionless microrotations
$Pr$ :	Prandtl number
$u, v, w$ :	Velocity components
$q_w$ :	Wall heat flux
$Re_r$ :	Local Reynolds number

$s$ :	Radial stretching rate
$T_s$ :	Surface temp. at the wall
$T_\infty$ :	Ambient temperature
$t_{wr}, t_{w\theta}, t_{wz}$ :	Wall couple stress.

## Greek Symbols

$\alpha, \beta, \gamma$ :	Material constants
$\alpha_c$ :	Concentration relaxation parameter
$\alpha_f$ :	Thermal diffusivity of the fluid
$\alpha_t$ :	Thermal relaxation parameter
$\delta$ :	Velocity slip parameter
$\Omega$ :	Angular velocity of the disk
$\omega_1, \omega_2, \omega_3$ :	Microrotation components
$\theta$ :	Dimensionless temperature
$\phi$ :	Dimensionless concentration
$\psi$ :	Dimensionless microrotation
$\Lambda$ :	Scaled stretching parameter
$\lambda_c$ :	Concentration relaxation time
$\lambda_e$ :	Thermal relaxation time
$\xi$ :	Dimensionless similarity variable
$\sigma$ :	Electrical diffusivity of fluid
$\rho_f$ :	Density of the base fluid
$\mu$ :	Absolute viscosity
$\tau_{zr}, \tau_{z\theta}$ :	Local shear stress.

## Data Availability

The data used to support the findings of this study are available from the author upon request

## Conflicts of Interest

The author declared that there is no potential conflict of interest with respect to the publication of this article.

## References

- [1] T. V. Kármán, "Über laminare und turbulente Reibung," *Journal of Applied Mathematics and Mechanics*, vol. 1, no. 4, pp. 233–252, 1921.
- [2] N. Bachok, A. Ishak, and I. Pop, "Flow and heat transfer over a rotating porous disk in a nanofluid," *Physica B*, vol. 406, no. 9, pp. 1767–1772, 2011.
- [3] M. Rashidi, N. Kavyani, and S. Abelman, "Investigation of entropy generation in MHD and slip flow over a rotating porous disk with variable properties," *International Journal of Heat and Mass Transfer*, vol. 70, pp. 892–917, 2014.
- [4] M. Sheikholeslami, M. Hatami, and D. Ganji, "Numerical investigation of nanofluid spraying on an inclined rotating disk for cooling process," *Journal of Molecular Liquids*, vol. 211, no. 3, pp. 577–583, 2015.
- [5] S. A. Wiese and C. Helwig, *Convective Heat Transfer from Rotating Disks Subjected to Streams of Air*, Springer, 1st edition, 2016.
- [6] T. Hayat, M. Rashid, M. Imtiaz, and A. Alsaedi, "Nanofluid flow due to rotating disk with variable thickness and homogeneous- heterogeneous reactions," *International Journal of Heat and Mass Transfer*, vol. 113, pp. 96–105, 2017.

- [7] A. Tulu and W. Ibrahim, "MHD slip flow of CNT-ethylene glycol nanofluid due to a stretchable rotating disk with Cattaneo-Christov heat flux model," *Mathematical Problems in Engineering*, vol. 2020, Article ID 1374658, 13 pages, 2020.
- [8] M. Ramzan, S. Riasat, J. D. Chung et al., "Upshot of heterogeneous catalysis in a nanofluid flow over a rotating disk with slip effects and entropy optimization analysis," *Scientific Reports*, vol. 11, no. 1, article 120, pp. 1–15, 2021.
- [9] S. S. Zhou, M. Bilal, M. A. Khan, and T. Muhammad, "Numerical analysis of thermal radiative Maxwell nanofluid flow over-stretching porous rotating disk," *Micromachines*, vol. 12, no. 5, p. 540, 2021.
- [10] D. Gamachu and W. Ibrahim, "Mixed convection flow of viscoelastic Ag-Al<sub>2</sub>O<sub>3</sub>/water hybrid nanofluid past a rotating disk," *Physica Scripta*, vol. 96, no. 12, article 125205, 2021.
- [11] A. M. Siddiqui, A. Sohail, K. B. Akram, and Q. A. Azim, "Flow of a fourth grade fluid between rotating disks," *Physics Letters*, vol. 34, no. 10, article 2050091, 2020.
- [12] A. Tulu and W. Ibrahim, "Mixed convection hybrid nanofluids flow of MWCNTs-Al<sub>2</sub>O<sub>3</sub>/engine oil over a spinning cone with variable viscosity and thermal conductivity," *Heat Transfer*, vol. 50, no. 4, pp. 3776–3799, 2021.
- [13] B. Jafeer and M. Mustafa, "A study of elasto-viscous fluid flow by a revolving disk with heat dissipation effects using HAM based package BVPh 2.0," *Scientific Reports*, vol. 11, no. 1, p. 4514, 2021.
- [14] H. Saia, R. Umme, I. Saba, K. Shamsa, and M. Bilal, "A numerical study of rotating Bödewadt flow of micropolar fluid over porous disk," *Mechanical Engineering*, vol. 236, no. 5, pp. 2147–2154, 2022.
- [15] U. Nazir, M. Sohail, M. M. Selim, H. Alrabaiah, and P. Kumam, "Finite element simulations of hybrid nano-Carreau Yasuda fluid with hall and ion slip forces over rotating heated porous cone," *Scientific Reports*, vol. 11, no. 1, article 19604, 2021.
- [16] M. I. Char and C. L. Chang, "Laminar free convection flow of micropolar fluids from a curved surface," *Journal of Physics D: Applied Physics*, vol. 28, no. 7, pp. 1324–1331, 1995.
- [17] M. Ramzan, J. D. Chung, and N. Ullah, "Partial slip effect in the flow of MHD micropolar nanofluid flow due to a rotating disk - a numerical approach," *Results in Physics*, vol. 7, pp. 3557–3566, 2017.
- [18] J. J. Shu and J. S. Lee, "Fundamental solutions for micropolar fluids," *Journal of Engineering Mathematics*, vol. 61, no. 1, pp. 69–79, 2008.
- [19] T. Ariman, M. A. Turk, and N. D. Sylvester, "Microcontinuum fluid mechanics—a review," *International Journal of Engineering Science*, vol. 11, no. 8, pp. 905–930, 1973.
- [20] C. Eringen, "Theory of micropolar fluids," *Journal of Applied Mathematics and Mechanics*, vol. 16, no. 1, pp. 1–18, 1966.
- [21] A. J. Willson, "Boundary layers in micropolar liquids," *Mathematical Proceedings of the Cambridge Philosophical Society*, vol. 67, no. 2, pp. 469–476, 1970.
- [22] A. C. Eringen, "Theory of thermomicrofluids," *Journal of Mathematical Analysis and Applications*, vol. 38, no. 2, pp. 480–496, 1972.
- [23] T. Ariman, M. A. Turk, and N. D. Sylvester, "Applications of microcontinuum fluid mechanics," *International Journal of Engineering Science*, vol. 12, no. 4, pp. 273–293, 1974.
- [24] S. Hussain, M. A. Kamal, and F. Ahmad, "The accelerated rotating disk in a micropolar fluid flow," *Applied Mathematics*, vol. 5, no. 1, article 42086, p. 7, 2014.
- [25] A. Yasmin, K. Ali, and M. Ashraf, "Study of heat and mass transfer in MHD flow of micropolar fluid over a curved stretching sheet," *Scientific Reports*, vol. 10, no. 1, p. 4581, 2020.
- [26] C. Zemedu and W. Ibrahim, "Nonlinear convection flow of micropolar nanofluid due to a rotating disk with multiple slip flow," *Mathematical Problems in Engineering*, vol. 2020, Article ID 4735650, 19 pages, 2020.
- [27] S. Hazarika and S. Ahmed, "Material behaviour in micropolar fluid of Brownian motion over a stretchable disk with application of thermophoretic forces and diffusion-thermo," *Journal of Naval Architecture and Marine Engineering*, vol. 18, no. 1, pp. 25–38, 2021.
- [28] U. Khan, A. Zaib, I. Pop, S. Abu Bakar, and A. Ishak, "Unsteady micropolar hybrid nanofluid flow past a permeable stretching/shrinking vertical plate," *Alexandria Engineering Journal*, vol. 61, no. 12, pp. 11337–11349, 2022.
- [29] M. S. Kausar, A. Hussanan, M. Waqas, and M. Mamat, "Boundary layer flow of micropolar nanofluid towards a permeable stretching sheet in the presence of porous medium with thermal radiation and viscous dissipation," *Chinese Journal of Physics*, vol. 78, pp. 435–452, 2022.
- [30] W. Ibrahim and A. Tulu, "Magnetohydrodynamic (MHD) boundary layer flow past a wedge with heat transfer and viscous effects of nanofluid embedded in porous media," *Mathematical Problems in Engineering*, vol. 2019, Article ID 4507852, 12 pages, 2019.
- [31] M. Waqas, M. Farooq, M. I. Khan, A. Alsaedi, T. Hayat, and T. Yasmeen, "Magnetohydrodynamic (MHD) mixed convection flow of micropolar liquid due to nonlinear stretched sheet with convective condition," *International Journal of Heat and Mass Transfer*, vol. 102, pp. 766–772, 2016.
- [32] G. Rasool, T. Zhang, A. J. Chamkha, A. Shafiq, I. Tlili, and G. Shahzadi, "Entropy generation and consequences of binary chemical reaction on MHD Darcy-Forchheimer Williamson nanofluid flow over non-linearly stretching surface," *Entropy*, vol. 22, no. 1, p. 18, 2019.
- [33] S. Akbar and M. Sohial, "Three dimensional MHD viscous flow under the influence of thermal radiation and viscous dissipation," *International Journal of Emerging Multidisciplinary*, vol. 1, no. 3, pp. 106–117, 2022.
- [34] K. Ali, A. A. Faridi, S. Ahmad, W. Jamshed, N. Khan, and M. M. Alam, "Quasi-linearization analysis for heat and mass transfer of magnetically driven 3rd-grade (Cu-TiO<sub>2</sub>/engine oil) nanofluid via a convectively heated surface," *International Communications in Heat and Mass Transfer*, vol. 135, article 106060, 2022.
- [35] M. B. Hafeez, M. Krawczuk, K. S. Nisar, W. Jamshed, and A. A. Pasha, "A finite element analysis of thermal energy inclination based on ternary hybrid nanoparticles influenced by induced magnetic field," *International Communications in Heat and Mass Transfer*, vol. 135, p. 106074, 2022.
- [36] W. Jamshed, M. R. Eid, S. M. Hussain et al., "Physical specifications of MHD mixed convective of Ostwald-de Waele nanofluids in a vented-cavity with inner elliptic cylinder," *International Communications in Heat and Mass Transfer*, vol. 134, article 106038, 2022.
- [37] S. M. Hussain, W. Jamshed, A. A. Pasha, M. Adil, and M. Akram, "Galerkin finite element solution for electromagnetic radiative impact on viscid Williamson two-phase nanofluid flow via extendable surface," *International Communications in Heat and Mass Transfer*, vol. 137, article 106243, 2022.

- [38] C. I. Christov, "On frame indifferent formulation of the Maxwell-Cattaneo model of finite-speed heat conduction," *Mechanics Research Communications*, vol. 36, no. 4, pp. 481–486, 2009.
- [39] A. Tulu and W. Ibrahim, "Spectral relaxation method analysis of Casson nanofluid flow over stretching cylinder with variable thermal conductivity and Cattaneo-Christov heat flux model," *Heat Transfer*, vol. 49, no. 6, pp. 3433–3455, 2021.
- [40] T. Hayat, S. Qayyum, M. Imtiaz, and A. Alsaedi, "Flow between two stretchable rotating disks with Cattaneo-Christov heat flux model," *Results in Physics*, vol. 7, pp. 126–133, 2017.
- [41] D. H. Doh, G. R. Cho, E. Ramya, and M. Muthamilselvan, "Cattaneo-Christov heat flux model for inclined MHD micropolar fluid flow past a non-linearly stretchable rotating disk," *Thermal Engineering*, vol. 14, article 100496, 2019.
- [42] A. Shafiq, A. B. Çolak, and T. N. Sindhu, "Analyzing activation energy and binary chemical reaction effects with artificial intelligence approach in axisymmetric flow of third grade nanofluid subject to Soret and Dufour effects," *Heat Transfer Research*, vol. 54, no. 3, 2023.
- [43] T. Naseem, U. Nazir, M. Sohail, H. Alrabaiah, E.-S. M. Sherif, and C. Park, "Numerical exploration of thermal transport in water-based nanoparticles: a computational strategy," *Case Studies in Thermal Engineering*, vol. 27, article 101334, 2021.
- [44] F. Wang, U. Nazir, M. Sohail, E. R. El-Zahar, C. Park, and P. Thounthong, "A Galerkin strategy for tri-hybridized mixture in ethylene glycol comprising variable diffusion and thermal conductivity using non-Fourier's theory," *Nanotechnology Reviews*, vol. 11, no. 1, pp. 834–845, 2022.
- [45] U. Shankar and N. B. Naduvinamani, "Magnetized impacts of Cattaneo-Christov double-diffusion models on the time-dependent squeezing flow of Casson fluid: a generalized perspective of Fourier and Fick's laws," *The European Physical Journal Plus*, vol. 134, no. 7, p. 344, 2019.
- [46] A. Tulu and W. Ibrahim, "Numerical analysis of heat and mass transfer flow of nanofluid over a moving wedge using spectral quasilinearization method," *International Journal of Applied Mathematics and Theoretical Physics*, vol. 5, no. 4, pp. 111–117, 2019.
- [47] S. E. Alhazmi, F. Wang, U. Nazir et al., "Utilization of modified fluxes on thermal and mass transportation in Williamson material," *Advances in Mechanical Engineering*, vol. 14, 2022.
- [48] M. Sohail, U. Nazir, Y.-M. Chu, H. Alrabaiah, W. Al-Kouz, and P. Thounthong, "Computational exploration for radiative flow of Sutterby nanofluid with variable temperature-dependent thermal conductivity and diffusion coefficient," *Open Physics*, vol. 18, no. 1, pp. 1073–1083, 2020.
- [49] S. S. Motsa, "A new spectral local linearization method for nonlinear boundary layer flow problems," *Journal of Applied Mathematics*, vol. 2013, Article ID 423628, 15 pages, 2013.
- [50] S. S. Motsa, Z. G. Makukula, and S. Shateyi, "Spectral local linearisation approach for natural convection boundary layer flow," *Mathematical Problems in Engineering*, vol. 2013, Article ID 765013, 7 pages, 2013.
- [51] A. Ishak, N. A. Yacob, and N. Bachok, "Radiation effects on the thermal boundary layer flow over a moving plate with convective boundary condition," *Meccanica*, vol. 46, no. 4, pp. 795–801, 2011.
- [52] G. Ramesh, G. S. Roopa, S. A. Shehzad, and S. U. Khan, "Interaction of  $\text{Al}_2\text{O}_3$ -Ag and  $\text{Al}_2\text{O}_3$ -Cu hybrid nanoparticles with water on convectively heated moving material," *Multidiscipline Modeling in Materials and Structures*, vol. 16, no. 6, pp. 1651–1667, 2020.
- [53] A. Tulu and W. Ibrahim, "Effects of second-order slip flow and variable viscosity on natural convection flow of (CNTs- $\text{Fe}_3\text{O}_4$ )/water hybrid nanofluid due to stretching surface," *Mathematical Problems in Engineering*, vol. 2021, Article ID 8407194, 18 pages, 2021.
- [54] L. N. Trefethen, "Spectral methods in MATLAB," in *Society for Industrial and Applied Mathematics*, Philadelphia, PA, USA, 1st edition, 2000.